High-Pressure oxidative coupling of methane on alkali metal catalyst – Microkinetic analysis and operando thermal visualization

Yu, Yuhang; Obata, Keisuke; Movick, William J.; Yoshida, Shintaro; Palomo, Jose; Lundin, Sean Thomas B.; Urakawa, Atsushi; Sarathy, S. Mani; Takanabe, Kazuhiro

Important note
To cite this publication, please use the final published version (if applicable).
Please check the document version above.

Contents lists available at ScienceDirect

Journal of Catalysis

Research article

High-Pressure oxidative coupling of methane on alkali metal catalyst – Microkinetic analysis and operando thermal visualization

Yuhang Yu [a], Keisuke Obata [a], William J. Movick [a], Shintaro Yoshida [a], Jose Palomo [b], Sean-Thomas B. Lundin [c], Atsushi Urakawa [b], S. Mani Sarathy [d], Kazuhiro Takanabe [a,e,*]

[a] Department of Chemical System Engineering, The University of Tokyo, 7-3-1 Hongo, Bunkyo-ku, Tokyo, 113-8656, Japan
[b] Department of Chemical Engineering, Delft University of Technology, Van der Maasweg 9, Delft 2629 HZ, the Netherlands
[c] Research Institute of Chemical Process Technology, National Institute of Advanced Industrial Science and Technology (AIST), 4-2-1 Nigatake, Miyagino-ku, Sendai 983-8551, Japan
[d] King Abdullah University of Science and Technology (KAUST), Clean Combustion Research Center (CCRC), Physical Sciences and Engineering Division (PSE), and KAUST Catalysis Center (KCC), 4700 KAUST, Thuwal 23955-6900, Saudi Arabia
[e] PRESTO, Japan Science and Technology Agency (JST), 4-1-8 Honcho, Kawaguchi, Saitama, 332-0012 Japan

ABSTRACT

To introduce promotional H_2O effects for both CH_4 rate and C_2 selectivity, the OH radical formation, catalyzed through H_2O activation with O_2 surface species, was critical for modeling selective $Mn-K_2WO_4/SiO_2$ catalysts. Based on our reported experimental evidence, which demonstrates the formation of H_2O_2 through surface alkali peroxide intermediate, the elementary reactions that account for the OH-mediated pathway were added into the microkinetic model. The advanced model adeptly replicated the promotional H_2O effects on both OCM rate and selectivity. The data from a low-pressure microkinetic study were treated isothermally, and extended for near-industrially relevant pressures up to 901 kPa. Thermal visualization using an infrared camera found substantial temperature increases at undiluted high-pressure conditions which caused C_2 selectivity to drop significantly. When the furnace temperatures were decreased after ignition, side reactions after O_2 depletion (e.g., hydrocarbon reforming) were suppressed, obtaining 13.7 (11.8) % yields at 19.9 % CH_4 conversion with 68.6 (59.1) % selectivities for C_{2-4} (C_2) at 901 kPa. The temperature was found to be the determining factor of C_2 yield which was perturbed by varying space velocity or CH_4/O_2 ratios. The optimum temperature for high-pressure conditions was predicted as 885 °C at 901 kPa. The study provides mechanistic and industrially relevant understandings for further OCM catalyst design and system application.

1. Introduction

Since the early work of Keller and Bhasin [1], the reaction mechanisms of oxidative coupling of methane (OCM) have been widely studied. Generally, the OCM reaction starts from methyl radicals that are activated from methane by catalyst surfaces, followed by recombination in the gas phase ($2CH_3\bullet \rightleftharpoons C_2H_6$) [2–4]. Through catalytic H-abstraction from ethane, subsequent hydrocarbons are formed, e.g., C_2 (C_2H_2, C_2H_4 and C_2H_6), C_3 (C_3H_6 and C_3H_8) and C_4 (C_4H_8 and C_4H_{10}) [5,6]. However, oxidation of methyl radicals and higher hydrocarbons leads to CO_x (CO and CO_2) via primary and secondary pathways [7–9], causing a limitation of C_{2-4} selectivity at high CH_4 conversion.

Various metal oxides, such as alkaline earth metal oxides [10,11] and rare earth metal oxides [12], were investigated to weaken the highly stable bond in methane to form methyl radical, where the lattice oxygen can abstract H from CH_4 [13]. La_2O_3-based catalysts, one of the most promising metal oxides, were reported with a maximum C_{2+} yield of 22 % and selectivity of 55 % under CH_4 and O_2 pressures of 81 and 20 kPa [14]. Higher surface area and stronger basic sites contribute to faster methane activation, which accelerates the second-order reaction of the CH_3 radical combination [15,16]. Due to the π-electrons in its unsaturated bond, however, the adsorption of C_2H_4 to the surface is stronger than that of CH_4, causing C_2H_4 oxidation and leading to low selectivity at high CH_4 conversion [5,7,17].

$(Mn-)Na_2WO_4/SiO_2$ catalyst has been studied extensively since Fang et al. [18,19], with a reported high C_2 yield of 26.4 % and selectivity of

* Corresponding author.
  E-mail address: takanabe@chemsys.t.u-tokyo.ac.jp (K. Takanabe).

80 % [20], significantly superior to the above-mentioned metal oxides. Otsuka et al. investigated various alkali peroxides to activate CH_4 and found that they are very reactive for the activation, but the reaction is stoichiometric, needing to be catalytic [21]. Upon investigating Na_2WO_4 supported on CeO_2, Lunsford and coworkers proposed that the catalyst activates CH_4 through transient active oxygen rather than the lattice oxygen as metal oxides [22]. The formation of Na_2O_2 over supported Na_2WO_4 at 800 °C was clearly detected via the in situ studies using ambient-pressure X-ray photoelectron spectrometer (AP-XPS) [23]. As the carrier of transient active oxygen, Na_2O_2 is proposed as the selective active site [23–26]. From the perspective of the mechanism, methane activation originates not only directly by surface oxygen species but also indirectly by highly reactive OH radicals produced from H_2O and O_2 through catalytically formed surface Na_2O_2, which contributes to a high selectivity and conversion rate [24,25]. The OH-mediated pathway was elucidated by the kinetic isotope effect[8], wherein H-abstractions were compared for CH_4, C_2H_4 and C_2H_6 [8,9] using in situ characterizations [23]. The water effect was studied at close-to-zero conversions to avoid the disturbances of self-produced H_2O by OCM. The OH radical can be formed through $O_2 + 2H_2O \rightleftharpoons 4OH\bullet$ with a reaction enthalpy of 650 kJ mol^{-1}. Further, Werny et al. mentioned that transient Na_2O is a highly active species [27]. Therefore, the active site is likely generated as $2Na_2O(s) + O_2 \rightleftharpoons 2Na_2O_2(s)$ and works as $Na_2O_2(s) + H_2O \rightleftharpoons Na_2O(s) + H_2O_2$, followed by $H_2O_2 \rightleftharpoons 2OH\bullet$ to generate the OH radical. This catalytic cycle typically happens very fast, so that $OH\bullet$ generation is often quasi-equilibrated with O_2 and H_2O pressures at OCM temperatures.

It has been shown that replacement of Na with K in the form of K_2WO_4/SiO_2 shows the same water effect and reaction mechanisms [28]. The main difference is the form of alkali tungstates: Na_2WO_4 melts at OCM temperature and makes a molten-salt state whereas K_2WO_4 seems to remain a nanoparticle state [28]. Surface K_2O_2 and KO_2 were evident by NAP-XPS experiment, which triggers for OH radicals to activate CH_4 in the gas phase, in a similar manner as Na_2O_2. Thus, transient active oxygen species in the form of $N_2O_2/K_2O_2/KO_2$ act as the active site for the OH-mediated pathway, contributing to the higher reaction rate and selectivity for alkali metal tungstate-based catalysts.

For industrial applications, OCM reactions are preferably conducted to further reduce the cost, such as saving compression work, reducing reactor size, etc., under high-pressure conditions without dilution. However, OCM reaction suffers from selectivity loss at elevated pressures [17,29,30], so it is necessary to understand the origins to reduce the losses quantitatively. It is well known that OCM reactions are strongly exothermic to cause hotspots [31–34]. This difficult-to-measure temperature rise might be one of the key factors causing the selectivity declining at high pressures with increased exotherms.

This study examines the elementary reaction mechanism of OCM and then uses this knowledge to explore industrially relevant high-pressure conditions, with Mn-K_2WO_4/SiO_2 taken as a model catalyst. A comprehensive microkinetic model was developed, based on our reported microkinetic modeling framework, for the alkali metal tungstate-based catalyst, including both surface-mediated and OH-mediated pathways [17,35–37]. Well-fitted conversions, selectivities and yields under 128 diluted conditions proved the reliability of the mechanism and kinetics data. The conditions were well distributed under different temperatures, space velocities and $CH_4/O_2/H_2O$ pressures. The model accurately described the effects of water on both reaction rate and product selectivity. The fundamental understandings were utilized to explore the relevant high-pressure industrial conditions. Operando thermal visualization was utilized to monitor and control the temperature distribution of the catalyst bed [38]. The catalyst bed temperature had sharp gradients, and the microkinetic model was utilized to predict the temperature of the reaction region. A sensitivity analysis was conducted to find decisive parameters from reaction pathways under both low and high pressures.

2. Methods

2.1. Catalyst preparation

SiO_2 (Sigma-Aldrich, Silica Gel Grade 643) was impregnated with $Mn(NO_3)_2 \cdot 6H_2O$ (FUJIFILM, 99.9 %) and K_2WO_4 (Alfa Aesar, 99.5 %) and dissolved in 6 ml of water. Then the solution was stirred and dried in ambient air at 100 °C to achieve 0.05 wt% and 2 wt% Mn contained 5 wt % K_2WO_4/SiO_2 for low-pressure and high-pressure conditions, respectively. The samples were further dried in a muffle furnace at 130 °C for 5 h, then calcined at 900 °C with a ramp rate of 5 °C min^{-1} and held for 9 h. The samples were sieved within a range of 0.25–0.50 mm after being pelletized under 40 kN for 20 s. Sn, In and Bi-doped samples were prepared by adding the corresponding precursors, $SnCl_4 \cdot 5H_2O$ (Sigma-Aldrich, 98 %), SnO_2 (Sigma-Aldrich, 99.9 %), $In(NO_3)_3 \cdot 3H_2O$ (FUJI-FILM, 99.9 %) and $Bi(NO_3)_3 \cdot 5H_2O$ (Sigma-Aldrich, 99.999 %), with the desired amount during wet impregnation.

2.2. Catalytic performance evaluation

Low-pressure measurements were performed in a U-shaped quartz flow reactor (4 mm I.D. and 6 mm O.D.) for the fitting of the micro-kinetic model. Catalysts (400 mg) were suspended by quartz wool. A bubbler with a temperature-controlled water jacket was utilized to introduce H_2O steam as a feed gas. To measure a large batch of data points, a Micro-GC (INFICON, 2-Module Micro GC Fusion) gas chromatograph was used to measure the products with each injection, equipped with an Rt-Molsieve 5A capillary column (0.25 mm, 10 m, Backflush 1.0 μL), Rt-Q-bond capillary column (0.25 mm, 3 m) and RT-Q-bond capillary column (0.25 mm, 12 m) with a thermal conductivity detector (TCD). In total, 128 conditions for low partial pressures were used to fit the surface kinetic data, which included CH_4 pressures of 5.0, 10, 20, 30 kPa, O_2 pressures of 0.56, 0.83, 1.67, 3.3 kPa, CH_4/O_2 ratios of 3–18, H_2O pressure of 0, 1.5 kPa, temperatures of 800, 850 °C and flow rates of 30, 60, 100, 150 ml min^{-1}. Ar was used as a balance gas. The key parameters of the catalyst and reactor are summarized in Table S1.

High-pressure measurements were conducted in a vertical fixed-bed flow reactor of a quartz tube (4 mm I.D. and 6 mm O.D.) by controlling a back pressure regulator manually. Catalysts (300 mg) were held by quartz wool with quartz rods (O.D. = 3.5 mm) on the lower and upper portions to minimize dead space. The concentration of effluent gas was measured every 20 min by a gas chromatograph (GC-2014, SHIMADZU) through a flame ionization detector (FID) with a GS-Gaspro column and TCD with a Shincarbon column. High-pressure conditions were explored including CH_4/O_2 ratios of 4–9, flow rates of 80–280 ml min^{-1}, furnace temperatures of 475–750 °C and total pressure of 101–901 kPa without dilution. In both cases, the temperature was measured through a K-type thermocouple controlled by an Omron controller (Omron, E5CC). Mass flow controllers (Alicat, MC-series) were utilized to control the inlet flow gas. For high-pressure water injection, a mass flow controller (Quantim) was used to control the flow rate of liquid water into a vaporizer which was set to 120 °C. O_2, CO, CO_2, H_2, CH_4, C_2H_2, C_2H_4, C_2H_6, C_3H_6, C_3H_8 and C_4H_8 were measured as products by GC after the removal of water vapor via a water trap in an ice box.

2.3. Characterizations

Operando thermal visualization was conducted to acquire the real-time temperature distribution of the catalyst bed using an infrared camera (Nippon Avionics Co., Ltd., InfReC H9000) through an open window on the furnace wall. The schematic diagram of the experimental setup and process of operando thermal visualization for high-pressure OCM reactions was shown in Figure S1. The results of Brunauer-Emmett-Teller (BET), X-ray Diffraction (XRD) and Scanning electron microscopy (SEM) can be found as Table S3, Figure S2 and Figure S3.

Table 1
Langmuir-Hinshelwood-based surface mechanism with optimized kinetic data.

No.	Reaction[a]	A^f	E_a^f	A^b	E_a^b
1[c]	$O_2 + * \rightleftharpoons O_2*$	0.151[b]	0	2.44×10^{11}	90.1
2[c]	$O_2* + * \rightleftharpoons 2O*$	1.75×10^{19}	30.0	1.75×10^{19}	7.70
3[c]	$H_2O + * \rightleftharpoons H_2O*$	0.521[b]	0	2.10×10^{13}	54.2
4[c]	$2OH* \rightleftharpoons H_2O* + O*$	1.75×10^{19}	174	1.75×10^{19}	107
5	$OH* + H \bullet \rightleftharpoons H_2O*$	1.05×10^{15}	40.0	1.75×10^{13}	363
6[c]	$H_2O* + O_2* \rightleftharpoons OH\bullet + OH* + O*$	5.09×10^{25}	190	1.75×10^{25}	0
7	$CH_3 + O* \rightleftharpoons CH_3O*$	$6.40 \times 10^{-5[b]}$	0	1.75×10^{13}	289
8	$CH_4 + * \rightleftharpoons CH_4*$	0.622[b]	0	1.75×10^{13}	21.0
9	$CH_4* + O* \rightleftharpoons CH_3* + OH*$	2.48×10^{23}	180	1.75×10^{19}	20.0
10	$CH_3* \rightleftharpoons CH_3\bullet + *$	1.75×10^{13}	0	$1.50 \times 10^{-3[b]}$	0
11	$C_2H_6 + * \rightleftharpoons C_2H_6*$	$1.04 \times 10^{-3[b]}$	0	1.75×10^{13}	44.8
12	$C_2H_6* + O* \rightleftharpoons C_2H_5* + OH*$	1.75×10^{19}	172	1.75×10^{19}	27.9
13	$C_2H_5* \rightleftharpoons C_2H_5\bullet + *$	1.75×10^{13}	0	$1.50 \times 10^{-6[b]}$	0
14	$C_2H_4 + * \rightleftharpoons C_2H_4*$	$8.35 \times 10^{-2[b]}$	0	1.75×10^{13}	135
15	$C_2H_4* + O* \rightleftharpoons C_2H_3* + OH*$	5.75×10^{20}	193	1.75×10^{19}	6.8
16	$C_2H_3* \rightleftharpoons C_2H_3\bullet + *$	1.75×10^{13}	29.2	$1.50 \times 10^{-6[b]}$	0
17	$C_2H_5* + O* \rightleftharpoons C_2H_4* + OH*$	1.75×10^{19}	0	1.75×10^{19}	426
18	$C_2H_3O* + O* \rightleftharpoons CH_2O* + CHO*$	1.75×10^{19}	0	1.75×10^{19}	432
19	$C_3H_6 + O* \rightleftharpoons C_3H_6O*$	$4.64 \times 10^{-3[b]}$	0	1.75×10^{13}	218
20	$C_3H_6O* + O* \rightleftharpoons C_3H_5O* + OH*$	5.75×10^{21}	105	1.75×10^{19}	94.6
21	$C_3H_5O* + O* \rightleftharpoons C_2H_3O* + CH_2O*$	1.75×10^{19}	145	1.75×10^{19}	187
22	$C_3H_8 + * \rightleftharpoons C_3H_8*$	$4.34 \times 10^{-2[b]}$	0	1.75×10^{13}	140
23	$C_3H_8* + O* \rightleftharpoons C_3H_7* + OH*$	1.75×10^{21}	169	1.75×10^{19}	31.2
24	$C_3H_7* + O* \rightleftharpoons C_3H_6* + OH*$	1.75×10^{21}	0	1.75×10^{19}	322
25	$C_3H_6* \rightleftharpoons C_3H_6 + *$	1.75×10^{13}	120	$4.64 \times 10^{-3[b]}$	0
26	$CH_3O* + O* \rightleftharpoons CH_2O* + OH*$	1.75×10^{19}	3.4	1.75×10^{19}	197
27	$CH_2O* + O* \rightleftharpoons CHO* + OH*$	1.75×10^{19}	23.5	1.75×10^{19}	176
28	$CHO* + O* \rightleftharpoons CO* + OH*$	1.75×10^{19}	0	1.75×10^{19}	224
29	$CO* + O* \rightleftharpoons CO_2* + *$	2.16×10^{24}	144	1.75×10^{19}	323
30	$CO + * \rightleftharpoons CO*$	$4.98 \times 10^{-8[b]}$	0	5.60×10^{12}	140
31	$CO_2 + * \rightleftharpoons CO_2*$	$1.00 \times 10^{-2[b]}$	0	1.75×10^{13}	69.9
32	$C_2H_3* + O* \rightleftharpoons C_2H_3O* + *$	1.75×10^{19}	45.4	1.75×10^{19}	208

[a] Species followed with "*" are adsorbed surface species, while a stand-alone "*" indicates an active site. [b] Initial sticking probability. The active site density is 2.15×10^{-10} mol cm^{-2}. [c] The catalytic contribution of OH-mediated pathway to produce OH radicals where the elementary reactions form the overall reaction of $O_2 + 2H_2O \rightleftharpoons 4OH\cdot$.

Units: E_a^f and E_a^b, kJ/mol. A, cm^2 mol^{-1} s^{-1} for reaction 2^b, 4^{f+b}, 6^f, 9^{f+b}, 12^{f+b}, 15^{f+b}, 17^{f+b}, 18^{f+b}, 20^{f+b}, 21^{f+b}, 23^{f+b}, 24^{f+b}, 26^{f+b}, 27^{f+b}, 28^{f+b}, 29^{f+b}, 31^{f+b}, 32^{f+b}; s^{-1} for reaction 1^b, 2^f, 3^b, 5^b, 7^b, 8^b, 10^f, 11^b, 13^f, 14^b, 16^f, 19^b, 22^b, 25^f, 30^b, 31^b; cm^3 mol^{-1} s^{-1} for reaction 5^f; cm^5 mol^{-2} s^{-1} for reaction 6^b, where f and b represent forward and backward reactions, respectively.

2.4. Microkinetic modeling

The gas-phase chemical kinetic model used KAM1-GS (KAUST-Aramco PAH Mech 1-GS) including a total of 3379 gas-phase reactions with 574 species [39]. The surface kinetic model, including 32 elementary catalytic reactions (see Table 1), was built based on Brønsted-Evans-Polanyi relationships [40], reaction enthalpy or thermodynamic data [35,37,41] and transition-state theory [37]. The values of activation energies/sticking probabilities/pre-exponential factors were optimized via the methodology reported by our previous work and other researchers [17,35,37,41]. CHEMKIN-PRO 17.0 software was utilized to simulate a standard one-dimensional (1D) plug flow reactor, coupled with a Python script to assist in the calculation and optimization.

The Thiele modulus and the catalyst's effectiveness are 0.575 and 0.999 calculated in support information, so mass transportation limitation was not considered in the model. The Weisz-Prater modulus also showed the pore diffusion limitation can be ignored (see supporting information, section " Weisz-Prater modulus".). The calculation of Mears' criterion indicates that the internal heat transfer limitation in the catalyst pellet is negligible for the experimental conditions in the kinetic study (see supporting information, section "Mears' criterion"). It is unnecessary to consider the pore volume and volume of the empty space in the reactor on top and below the catalyst bed in the model. For low-pressure conditions, pore volume can be included in the void fraction of the pseudo-homogeneous model. The Theile modulus and Weisz-Prater modulus in support information showed that the mass transportation limitation is negligible even at high pressures. Additionally, influence of the empty space on top and below the catalyst bed was also

negligible because the quartz rod was used to minimize the dead space on top and below the catalyst bed during our catalytic OCM experiment. For high-pressure conditions, pore volume can be included in the void fraction of the pseudo-homogeneous model, which is the same as low-pressure conditions. Additionally, although higher pressure will cause higher CH$_4$ conversion rate even without catalysts, the CH$_4$ conversion rate was minimized by using the quartz rod. Because the empty space on the top of catalyst bed was much shorter than 6 cm, its influence was also negligible for high-pressure conditions as shown in Figure S4. Detailed information can be found in our previous work on an improved Langmuir-Hinshelwood-based microkinetic model [17]. Catalyst and reactor parameters were listed in Table S1.

2.5. Criteria function for temperature estimation

To calc ulate the error between calculation and experiment for the high-pressure condition, the following criteria function was used as the goal function in particle swarm optimization algorithm [42,43]. The fitted parameters were CH$_4$ conversion, C$_2$H$_6$ selectivity, C$_2$H$_4$ selectivity, CO selectivity, CO$_2$ selectivity and C$_{2-3}$ yield.

$$G(T, \Gamma) = \sum_{i=1}^{n_{high}} E_i^T w_E E_i \xrightarrow{T, \Gamma} \min \qquad (1)$$

$$E_{ij} = f_{ij}(x_i; \beta) - Y_{ij} \qquad (2)$$

$$w_E = \sigma_E^{-2} \qquad (3)$$

where T is the reaction temperature; Γ is the site density of the catalyst surface; n_{high} is the number of observations of high-pressure conditions; E_i is the error matrix of the ith observation, $p \times 1$; E_{ij} is the jth response from the ith observation ($0 < j \leq p$); p is the number of responses; w_{Ei} is the inverse of the error covariance matrix, σ_{Ei}^{-2}, acquired from the difference between low-pressure calculations and experiments, $p \times p$; Y_{ij} is the jth response of the ith observation.

3. Results and discussion

3.1. Reaction pathways and microkinetic analysis

Based on the same elementary surface reactions as our reported La$_2$O$_3$-CeO$_2$ catalyst, [17] the explored elementary reactions of the OH-mediated pathway (reactions (1), 2, 3, 4, 6) via alkali peroxide intermediate were added into the microkinetic model. The surface mechanism, including the above-mentioned surface-mediated and OH-mediated pathways, was summarized in Table 1 together with the kinetic data. The developed model successfully reproduced the promotional H$_2$O effects that have never been reproduced by other models before. Even regardless of the promotional H$_2$O effect, the model also provides the highest accuracy among the models on Mn-K$_2$WO$_4$/SiO$_2$.

Figure S5 shows the parity plots of the comprehensive microkinetic model for CH$_4$ conversion, CO, CO$_2$, C$_2$H$_4$, C$_2$H$_6$ selectivities and C$_{2-3}$ yield under wide ranges of diluted conditions on Mn(0.05 wt%) K$_2$WO$_4$(5 wt%)/SiO$_2$. The model accurately predicts both wet (with H$_2$O introduced) and dry (without H$_2$O introduced) conditions. Positive effects of water on OCM reaction rates and C$_{2-3}$ selectivities were present under all conditions. C$_{2-3}$ selectivities under wet and dry conditions are presented in Fig. 1 as functions of CH$_4$ conversion. In wet conditions, 1.5 kPa H$_2$O was introduced as a reactant to enhance the OH-mediated pathway in the presence of O$_2$. The difference in selectivities between wet and dry conditions was narrowed with increasing CH$_4$ conversion, as H$_2$O is produced in both dry and wet conditions. It can be seen from $r_{CH_4,OH} = k'' P_{CH_4} P_{O_2}^{1/4} P_{H_2O}^{1/2}$ that the CH$_4$ activated by the OH-mediated pathway is kinetically half-order of the H$_2$O pressure [8,9], indicating that the enhancement from the water effect will reduce with increasing H$_2$O pressures. The amount of produced H$_2$O increases at higher CH$_4$ conversions, causing the selectivity differences between wet and dry
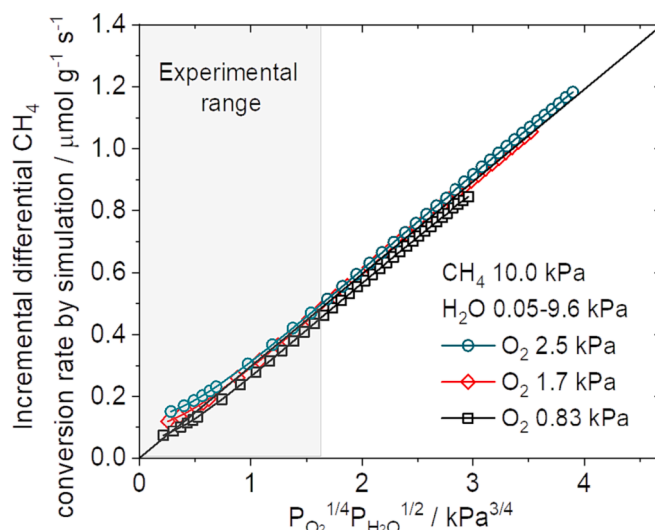

Fig. 2. Incremental differential CH$_4$ conversion rate (calculated differences in rates with and without H$_2$O) as a function of $P_{O_2}^{1/4} P_{H_2O}^{1/2}$ (the experimental range of 0–1.65 kPa$^{3/4}$) under CH$_4$ pressure of 10.0 kPa, H$_2$O pressures of 0.05–9.6 kPa and O$_2$ pressures of 0.83, 1.7, 2.5 kPa, catalyst amount of 100 mg, 850 °C, flow rate of 150 ml min^{-1}, total pressure of 101 kPa, Ar balance, without O$_2$ depletion.

conditions to decrease.

The C$_{2-3}$ selectivity of alkali metal tungstate-based catalysts, e.g., (Mn-)K$_2$(or Na$_2$)WO$_4$/SiO$_2$, is much higher than metal oxide catalysts, e. g., La$_2$O$_3$-CeO$_2$, suggesting that the reaction proceeds via different mechanism. Metal oxide catalysts tend to overoxidize CH$_4$ and the subsequent products to CO$_x$ because of the surface-dominated mechanism of metal oxides. Although OH radicals were found to be produced on La$_2$O$_3$ catalysts at ca. 900 °C by Lunsford [44,45], the reaction temperatures of 550–750 °C used for this catalyst are not high enough to produce a significant amount of OH radicals. In addition, the gas-phase contribution of OCM has much lower reaction rates compared to surface reactions. In the case of alkali metal tungstate-based catalysts, however, the reaction temperature is high enough (850 °C) to produce OH radicals. Also, the slow surface reaction rate makes the gas-phase
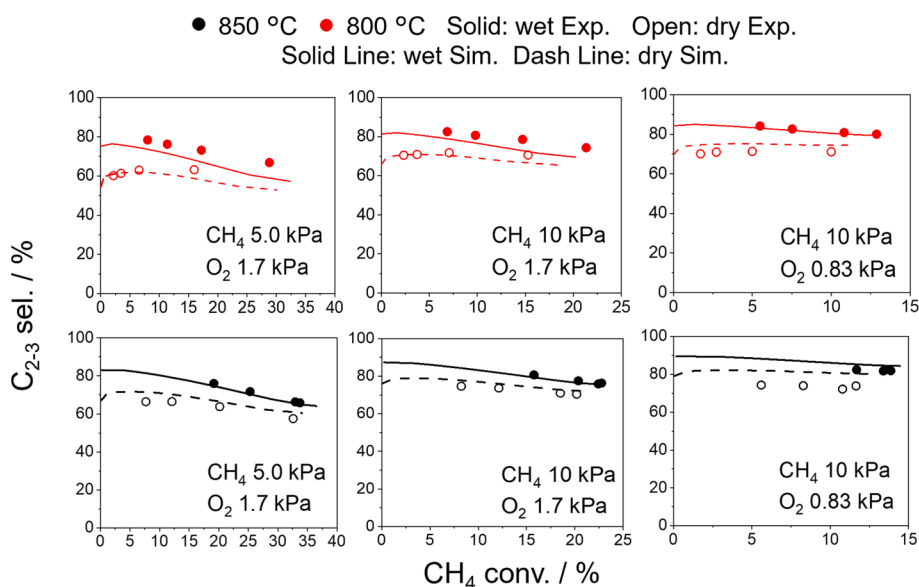

Fig. 1. The selectivity of C$_{2-3}$ as a function of CH$_4$ conversion with or without H$_2$O addition at the inlet, between the calculated and measured results (128 conditions) under CH$_4$ pressures of 5.0 and 10 kPa, O$_2$ pressures of 0.83 and 1.7 kPa, CH$_4$/O$_2$ ratios of 3, 6 and 12, H$_2$O pressure of 0 and 1.5 kPa, Ar balance, temperatures of 800, 850 °C and flow rates of 30, 60, 100, 150 ml min^{-1}. Wet: with H$_2$O introduced; dry: without H$_2$O introduced as a feed gas.

contribution significant. The produced OH radicals can activate CH_4 to $CH_3\bullet$ in the gas phase, which has been shown to be more selective than other H-abstractors, e.g., HO_2, O, O_2 [8].

Fig. 2 shows the simulated incremental differential CH_4 conversion rate, $r_{CH4, OH}$, which is calculated by the differences between rates with and without H_2O through the microkinetic model, as a function of O_2 and H_2O pressures. The surface elementary reaction 6 plays an essential role in the model to keep consistent with kinetic behaviors where the reaction orders of O_2 and H_2O are expected to be 0.25 and 0.5, respectively. The elementary reaction describes the reaction between adsorbed O_2 and adsorbed H_2O molecules to produce OH radicals, which is combined with the adsorption of oxygen molecules (reaction (1), dissociation of oxygen surface species (reaction (2), adsorption of water molecules (reaction (3) and combination of hydroxyl surface species (reaction (4) to form the overall reaction of $O_2 + 2H_2O \rightleftharpoons 4OH\bullet$. This is consistent with our previous experimental findings on similar catalysts.[8,9] The overall CH_4 conversion rates can be described by

$$r_{CH_4} = r_{CH_4,\text{surface}} + r_{CH_4,OH} = k'P_{CH_4}P_{O_2}^{1/2} + k''P_{CH_4}P_{O_2}^{1/4}P_{H_2O}^{1/2} \qquad (4)$$

which consisting of surface-mediated and OH-mediated pathways.

To quantitatively compare the difference between alkali metal tungstate-based (wet/dry) and metal oxide catalysts, apparent pseudo-first-order rate constants of the main reaction pathways were calculated using the developed microkinetic model as shown in Table 2. In the table, "k_n" (n = 1–5) is the pseudo-first-order rate constant for hydrocarbon species ($r = k_n$ [hydrocarbon]) independent of O_2 pressure, which can be seen from the pathway (CH_4 to C_2H_6) in Scheme 1. The analysis methodology refers to the literature [8,9]. By utilizing these constant ratios (e.g., k_i/k_1), for example, the attainable OCM yield can be obtained as a simplified estimate. It is difficult to get the exact rate constants for all the elementary steps established in our microkinetic model because our model contains too many reactions to even describe a conversion of single component, around 4000 reactions in total. Instead, the comparison of these values among the different catalysts, or with or without H_2O addition conditions would provide valuable information towards OCM selectivity.

Rate constant ratios were calculated to evaluate the primary oxidation (k_2/k_1) and secondary oxidation (k_3/k_1, k_4/k_1, k_5/k_1). The k_4/k_1 ratio was ignored because C_2H_6 is converted to C_3 through C_2H_5. The overall methane conversion rate constant of La_2O_3-CeO_2 is 91.9 times higher than that of Mn-K_2WO_4/SiO_2 under dry conditions and 32.3 times higher than that of Mn-K_2WO_4/SiO_2 under wet conditions. However, the predicted attainable C_{2-4} yield and selectivity on La_2O_3-CeO_2 are merely 10.5 and 59.3 % while Mn-K_2WO_4/SiO_2 exhibits the much better C_{2-4} yield and selectivity of 17.2 and 75.2 % with the O_2 depletion under CH_4 and O_2 pressures of 10.0 and 1.67 kPa. The strong surface oxidation by surface oxygen on La_2O_3-CeO_2 leads to the overoxidation of $CH_3\bullet$ as well as C_{2-3} products into CO_x, which can be seen from larger values for k_2/k_1, k_3/k_1, k_5/k_1 for La_2O_3-CeO_2 catalyst than Mn-K_2WO_4/SiO_2. These observations accurately reflect the fact that C_2 or higher
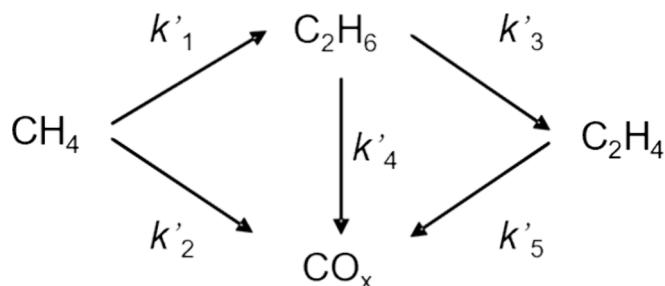
Scheme 1. Reaction network of OCM with peudo-first-order rate constants.

hydrocarbons adsorb strongly on La_2O_3-CeO_2 relative to CH_4, consistent with the previous claims [5,7,17]. For Mn-K_2WO_4/SiO_2, the contribution of the overoxidation of the surface-mediated pathway can be minimized by enhancing the OH-mediated pathway where C–H bond abstraction reactions happen in the gas phase. The addition of H_2O further enhanced the OH-mediated pathway. With the introduction of 1.5 kPa H_2O, k_1 increases by 2.85 times while k_2 and k_5 increase by only 1.62 and 1.14 times, respectively. Faster $CH_3\bullet$ production accelerates the coupling to C_2H_6 through the second-order reaction in the gas phase, while overoxidation reactions of methyl radical and C_2 products do not significantly increase, contributing to the higher selectivity at elevated conversion.

3.2. Operando thermal visualization of high-pressure OCM

Elevating operating pressures is critical for the industrial application of OCM process. The relevance between reaction exothermicity and temperature change was explored real time using an infrared thermometer that measures the catalyst bed temperature distribution through a window of the special reactor at the total pressure of 901 kPa. The correlation fundamental understandings were newly utilized to control the temperature distribution of catalyst bed to improve the C_{2-4} yield. The microkinetic model, developed from low-pressure conditions, was used to assist the temperature prediction for high-pressure OCM process.

To monitor the catalyst's temperature distribution, an operando thermal visualization platform was established by using an infrared camera through an open window on the furnace wall (Fig. 3a). The open window in the furnace wall can accelerate the heat dissipation to the outside of the furnace. However, the temperature inside the furnace will still be maintained around the set point that is controlled by the temperature controller via the thermocouple as shown in Figure S1. Because OCM reaction is exothermic, the temperature of hotspot in the catalyst bed can be much higher than the set temperature during OCM process. Therefore, the enhancement of heat dissipation through the open window will cause the decrease of maximum temperature of temperature profiles in the catalyst bed. The measured temperature was validated by observing the catalyst bed without reactions as shown in Figure S6.

Table 2
Apparent first-order rate constants (s^{-1}) and their ratios calculated from rate of production (ROP) analysis among La_2O_3-CeO_2, Mn-K_2WO_4/SiO_2 (0 kPa H_2O), Mn-K_2WO_4/SiO_2 (1.5 kPa H_2O) under CH_4 pressure of 10.0 kPa, O_2 pressure of 1.7 kPa, O_2 conversion of 5 %.

Catalysts	k_1	k_2 (k_2/k_1)	k_3 (k_3/k_1)	k_4 (k_4/k_1)	k_5 (k_5/k_1)
La_2O_3-CeO_2[a]	1.0×10^2	27 (0.26)	1.2×10^3 (12)	0.23 (0.0022)	1.6×10^3 (16)
Mn-K_2WO_4/SiO_2[b]	1.1	0.25 (0.22)	9.6 (8.7)	0.040 (0.036)	10 (9.2)
Mn-K_2WO_4/SiO_2[c]	3.2	0.40 (0.13)	23 (7.2)	0.083 (0.026)	12 (3.7)

[a] Calculated based on our previous model [17] on La_2O_3-CeO_2 under 750 °C;
[b, c] Calculated under 850 °C without (b) and with (c) 1.5 kPa water vapor addition as an inlet gas.
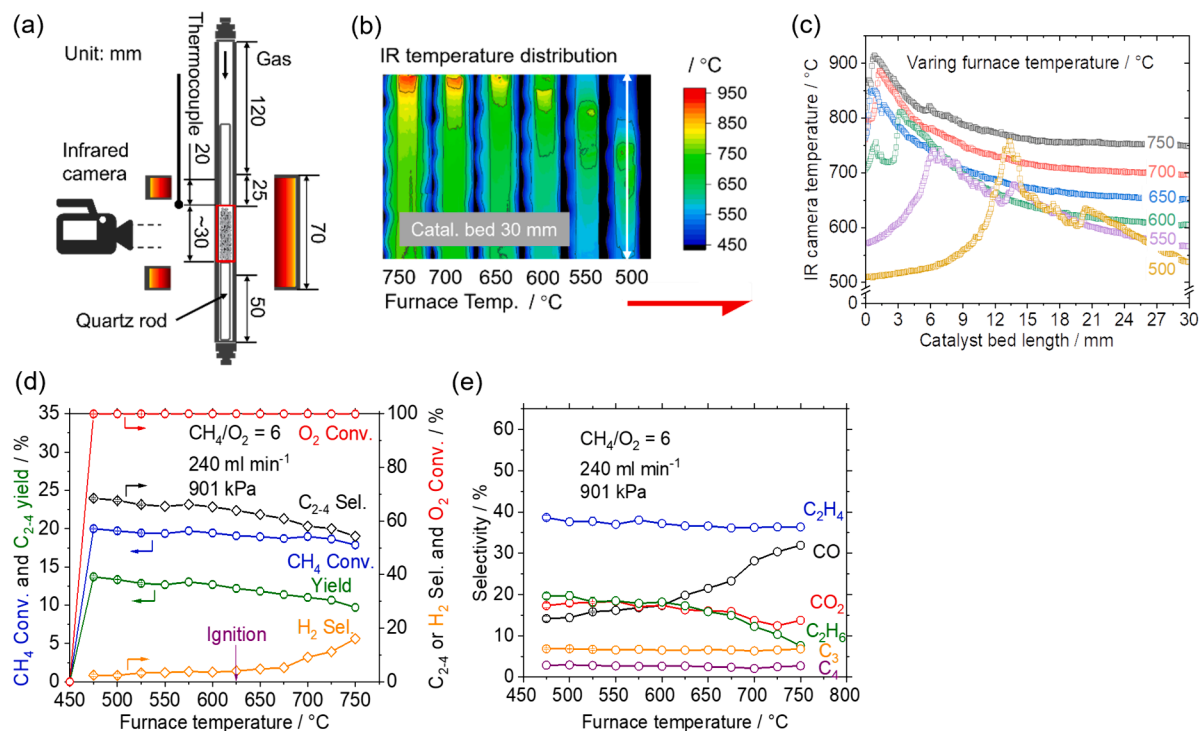
Fig. 3. (a) Schematic diagram of operando thermal visualization; (b) temperature distribution and (c) temperature profiles of the catalyst bed under furnace temperatures varying from 750 to 450 °C during the light-off procedure; (d) CH_4 and O_2 conversion, C_{2-4} yield, C_{2-4} and H_2 selectivity and (e) selectivity of each carbon product as a function of the furnace temperature at CH_4/O_2 ratio of 6, flow rate of 240 ml min^{-1} without dilution gas, catalyst amount of 300 mg, pressure of ca. 901 kPa. Multiple points were measured at the temperature from 525 to 475 °C, plotted with error bars.

The steady state multiplicity was observed as shown in Figure S7. As the furnace temperature was increased up to 625 °C, the reaction was ignited. The furnace temperature was continuously raised up to 700 °C, and then decreased until the reaction stopped. The temperature hysteresis can be clearly seen that the furnace temperature can go much lower than the light-on one. To optimize reaction temperatures, the
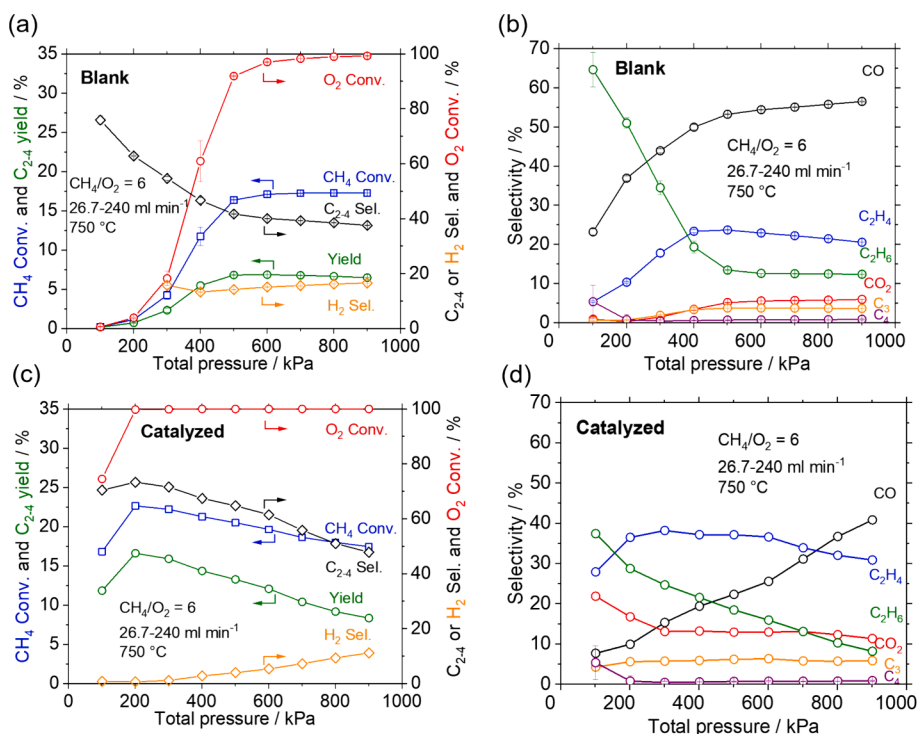
Fig. 4. (a) CH_4 and O_2 conversion, C_{2-4} yield, C_{2-4} and H_2 selectivity and (b) selectivities of carbon products as a function of total pressures, conducted in a blank reactor; (c) CH_4 and O_2 conversion, C_{2-4} yield, C_{2-4} and H_2 selectivity and (d) selectivities of carbon products as a function of total pressures, using 100 mg Mn(2 wt%) K_2WO_4(5 wt%)/SiO_2 and 3.5 mm O.D. quartz rod in the reactor. All conditions vary from 101 to 901 kPa with a CH_4/O_2 ratio of 6 at a furnace temperature of 750 °C with flow rates of 26.7–240 ml min^{-1} to keep the same residence time.

furnace temperature was initially increased to 750 °C, with ignition of the OCM reaction occurring at ca. 625 °C, then decreased by every 25 °C to measure the results until extinction (450 °C). The hot spot formed by strong reaction heat from OCM can be clearly seen in Fig. 3(b). Fig. 3(c) shows the temperature profiles along the central axis of the catalyst beds, with significant temperature increases visible. The observed maximum temperature reaches ca. 750 °C at the furnace temperature of 500 °C, indicating the observed temperature increase can be as high as ca. 250 °C. When one considers the thermal resistance inside the catalyst bed, the actual maximum reaction temperature is likely even higher. During the extinction procedure with the furnace temperature reduced from 750 to 450 °C, the hot spot moved from the beginning to the end of the catalyst bed. At lower furnace temperatures, the inlet gas requires a longer bed length to ignite the reaction. Meanwhile, the observed maximum temperature decreases because the inlet temperature is lower. Fig. 3(d) and (e) shows that C_{2-4} selectivity and yield increase, but H_2 and CO selectivities decrease with the decreasing furnace temperatures. Hydrocarbon reforming after O_2 depletion might be inhibited by decreasing the temperatures [46]. From 600 °C to 475 °C, the C_{2-4} (C_2) yield were further improved up to the maximum, ca. 13.7 (11.8) % at 19.9 % CH_4 conversion with 68.6 (59.1) % selectivities. The catalyst shows stable performance for 20 h, at least in the timescale of our microkinetic study even at high pressure, as can be seen in Figure S8. For future perspective, the detailed stability study for high-pressure OCM reaction should be conducted, which requires detailed investigation on heat management by not only catalyst composition and its nature but also the reaction conditions including furnace temperature, heat dissipation, and exothermicity influenced by space velocity. Lowering the furnace temperature to 475 °C minimized the unselective gas-phase reactions and thereby improve the C_{2-4} yield.

Unselective gas-phase reactions were found to be greatly enhanced by elevated pressures in the blank reactor as shown in Fig. 4. Operando thermal visualization was also conducted for the blank reactor as presented in Figure S9. The unselective gas-phase reactions became faster because of the higher reaction rates at higher pressures, which completely cosumed the reactant O_2 at the pressure of higher than 701 kPa at 750 °C as shown in Fig. 4(a) and (b). Different from the above experiments using blank reactors, Fig. 4(c) and (d) show the experimental results in the presence of Mn-K_2WO_4/SiO_2 catalyst. At 750 °C furnace temperature, O_2 is depleted at much lower pressure of 201 kPa with the catalyst, compared to that of 701 kPa for the blank reactor as shown in Fig. 4(a) and (b), indicative of enhanced rates with the catalyst. Both C_{2-4} yield and selectivity are enhanced by addition of surface reactions, but they decrease significantly with increasing pressure. H_2 and CO selectivities increase with increasing pressure, which reach the highest 11.1 and 48.8 % at 901 kPa, respectively, close to those of blank reactor (15.6 and 56.5 %). Clearly, elevating the reactant pressures greatly accelerates the unselective gas-phase reaction, reducing the relative contribution of surface reactions to cause the loss of C_{2-4} yield and selectivity.

Unlike low-pressure conditions, additional H_2O did not significantly improve selectivities for high-pressure conditions (see Figure S10). This is because the produced H_2O have sufficient pressure to realize the OH-mediated pathway and caused saturated impact on the selectivity under the molar fraction of produced H_2O of ca. 20 %. Fig. 1 shows that the difference between dry and wet conditions becomes smaller at higher conversions, consistent with the larger H_2O pressures at higher conversions.

The high exothermicity of OCM induces a temperature profile along the catalyst bed, making the effect of different catalyst compositions difficult to determine. As an example, various catalysts with different compositions (e.g., Sn-, Bi-, In-doped, Mn contained) and contents were tested under a total pressure of ca. 901 kPa without dilution and a furnace temperature of 750 °C as listed in Table S2. Sn addition into Mn-K_2WO_4/SiO_2 showed better performance than without Sn addition. However, detailed study among Mn(2 wt%)/K_2(or Na_2) WO_4(5 wt
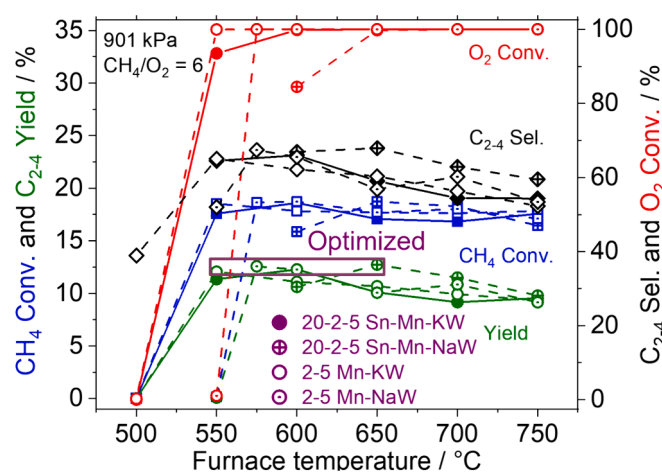

Fig. 5. CH_4 and O_2 conversion, C_{2-4} yield, C_{2-4} selectivity under furnace temperatures varying from 750 to 500 °C during light-off procedure, pressure of 901 kPa, CH_4/O_2 ratio of 6, flow rate of 240 ml min^{-1} and catalyst amount of 200 mg on Mn(2 wt%)Na_2WO_4(5 wt%)/SiO_2, Mn(2 wt%)K_2WO_4(5 wt%)/SiO_2, Sn(20 wt%)Mn(2 wt%)Na_2WO_4(5 wt%)/SiO_2 and Sn(20 wt%)Mn(2 wt%) K_2WO_4(5 wt%)/SiO_2.

%)/SiO_2 with and without 20 wt% Sn addition revealed that the yield and selectivity of C_{2-4} are almost the same at optimized furnace temperatures (Fig. 5). Additionally, Sn-doped catalysts required higher furnace temperatures before light-off than those without Sn, suggesting that their conversion rates were lower, which decreased the reaching temperature caused by the exothermic reaction compared with the catalyst without Sn. The furnace temperature comprised in Table S2 is therefore too high from the optimum. This result suggests that Sn addition essentially causes the dilution of active sites without causing substantial loss of selectivity. Therefore the Sn addition may be useful to control the number of active site per given volume of the reactor, so that the temperature per volume can be tuned. Additionally, temperature reached by the exothermic reaction is critical and sensitive to determine the performance, reflecting the achievable reaction rate by a given catalyst composition. Dramatic temperature increases during high-pressure OCM reactions were predicted previously on La_2O_3-CeO_2 [17]. Therefore, temperature is an essential factor to investigate.

Flow rates (see Fig. 6) and CH_4/O_2 ratios (see Figure S11) were varied to study their effects on catalytic performances, while furnace temperatures were controlled to maintain a maximum temperature around 700 °C. From Fig. 6(a) and (b), CH_4 conversion, C_{2-4} yield and selectivities decrease with decreasing flow rates, especially 80 ml min^{-1}. Lower flow rates give smaller reaction heating rates, while heat dissipation is nearly constant with the constant maximum temperatures (Fig. 6d and e). Thus, a lower flow rate requires higher furnace temperatures to provide more heat to maintain the same maximum temperature. If the furnace temperature becomes higher than 550 °C at 901 kPa, however, unselective gas-phase reactions become significant in dead space (e.g., quartz wool before the catalyst bed). From 160 to 280 ml min^{-1}, catalytic performances are almost the same, with unselective gas-phase reactions minimized because of low furnace temperatures. CH_4/O_2 ratios show similar effects (see Figure S11). Both cases indicate that reached temperature is the more important OCM parameter that is influenced by flow rates and CH_4/O_2 ratios for high-pressure catalytic OCM reactions.

3.3. Sensitivity analysis for the model

The sensitivities were calculated to analyze the contributions of surface-mediated and OH-mediated pathways at both low and high-pressure conditions. They can also be utilized to correct the validation results between calculation and experiment. Introduced surface
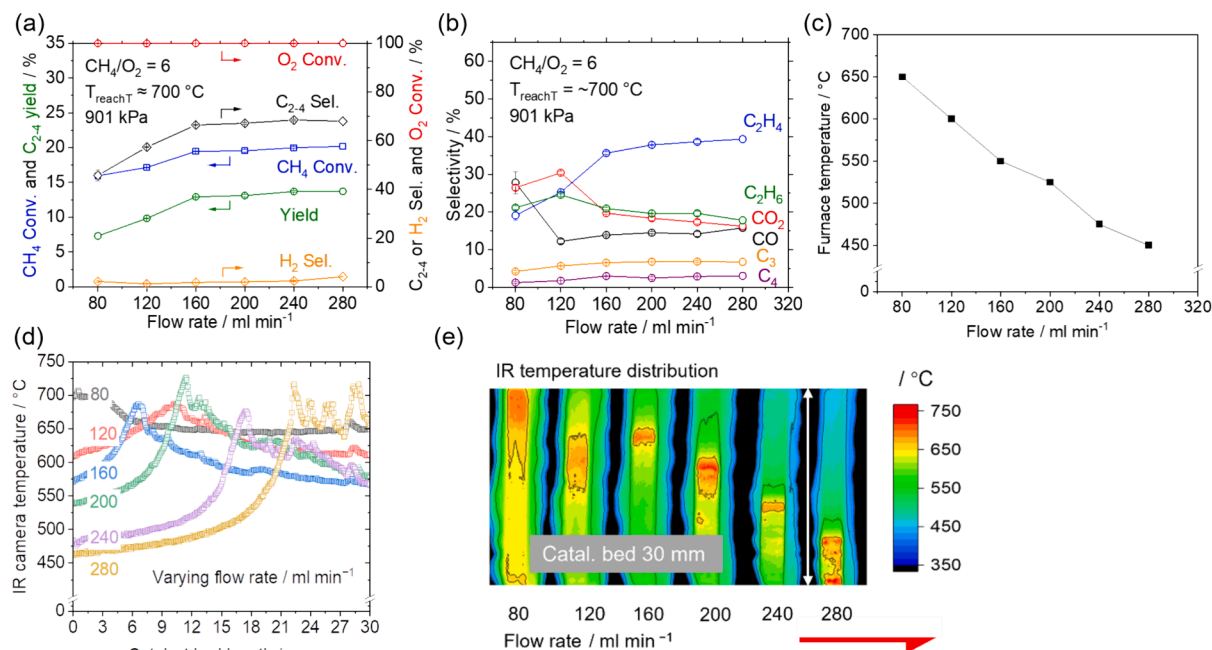
Fig. 6. (a) CH$_4$ and O$_2$ conversion, C$_{2-4}$ yield, C$_{2-4}$ and H$_2$ selectivity, (b) selectivities of carbon products and (c) furnace temperature as a function of flow rates from 80 to 280 ml min^{-1} at the maximum temperature of ca. 700 °C, CH$_4$/O$_2$ ratio of 6 without dilution, catalyst amount of 300 mg, pressure of ca. 901 kPa; (d) axial temperature profiles and (e) temperature distributions of the catalyst bed during the variation in flow rates. Multiple points were measured for each condition, plotted with error bars.
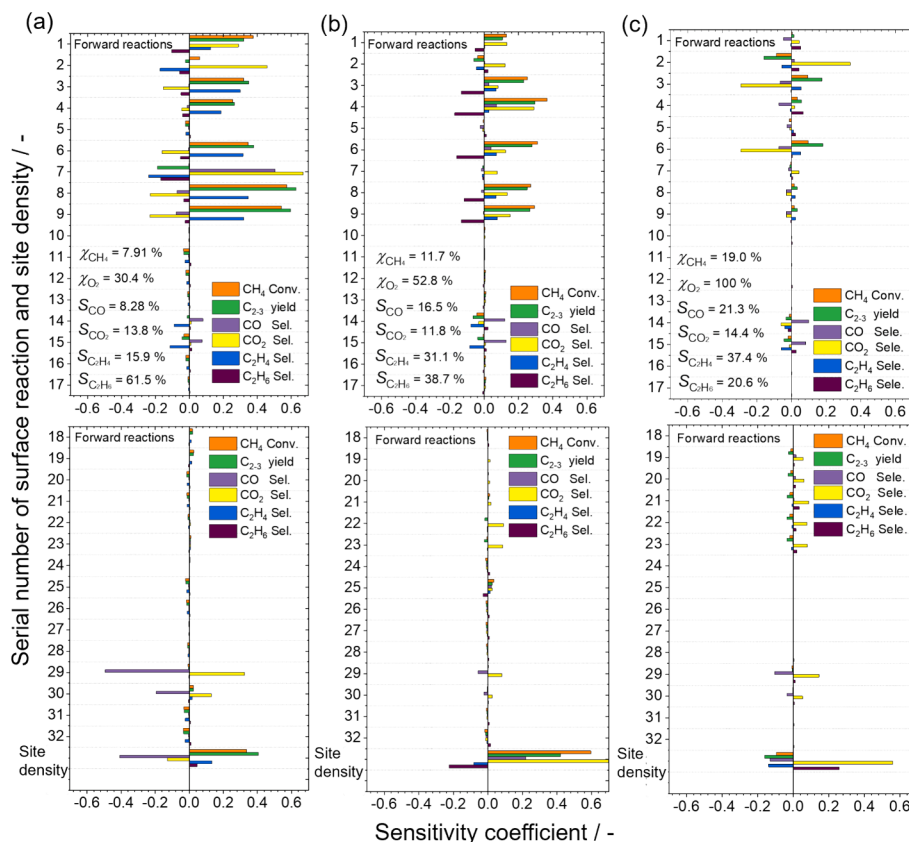
Fig. 7. Sensitivity coefficients of the forward surface reactions in Table 1 as well as site density for the model under (a) CH$_4$ pressure of 10.0 kPa, O$_2$ pressure of 1.67 kPa, temperature of 850 °C, total pressure of 101 kPa with Ar balance, flow rate of 150 ml min^{-1}, catalyst amount of 400 mg; CH$_4$ pressure of 772 kPa, O$_2$ pressure of 129 kPa, temperature of 885 °C, total pressure of 901 kPa, flow rate of 240 ml min^{-1}, (b) catalyst amount of 10 mg without O$_2$ depletion and (c) catalyst amount of 30 mg with O$_2$ depletion.

elementary steps listed in Table 1 exhibit different sensitivities on the OCM performance modeling. The sensitivity coefficients of the reactions were calculated based on the defined equations described in supporting information to analyze the influence of forward (Fig. 7) and backward (Figure S12) reaction rate constants together with active site density of catalyst in a given volume on CH_4 conversion, C_{2-3} yield and selectivities of CO, CO_2, C_2H_4 and C_2H_6. Fig. 7(a) shows the low-pressure diluted case at CH_4 conversion of ~ 8 % where reactions 1, 2, 3, 4, 6 (OH-mediated), 7, 8, 9 (surface-mediated), 14, 15, 29, 30 are found to be more sensitive than other reactions. Oxygen adsorption and methane activation are the very first steps of OCM reactions, which explain the high sensitivities of these reactions. Additionally, primary oxidation from $CH_3\bullet$ to CO_x (reaction 7) and secondary oxidation from CO to CO_2 (reaction 29) on the surface play an important role. Fig. 7(b) shows that the above surface reactions at CH_4 conversion of ~ 11 % are still the most sensitive as CH_4 pressure was increased from 10 to 772 kPa, but they are less sensitive because the contribution of the catalyst surface might be decreased by gas-phase reactions. Fig. 7(c) shows that the reactions at CH_4 conversion of ~ 19 % with O_2 depletion become more insensitive under 901 kPa except for reactions 2, 3 and 6, which come from the OH-mediated pathway. This shows the importance of the pathway on the selectivities even under O_2-depleted conditions.

In contrast, the site density remains sensitive among various conditions. Increased site density increases both CH_4 conversion and C_{2-3} yield in Fig. 7(a) and (b) because increasing site density can contribute to higher total reaction rates at a constant specific surface area. After O_2 depletion, as Fig. 7(c) shows, however, increasing site density decreases CH_4 conversion and C_{2-3} yield. Higher site density consumes O_2 faster, leaving a longer bed length without O_2 presence. Because the current surface mechanism includes no reaction after O_2 depletion while the gas phase mechanism tends to produce CH_4 from C_{2-3} reversely [46], CH_4 conversion and C_{2-3} yield decreased slightly after O_2 depletion. Side reactions will convert C_{2-3} to CO_2 (e.g., hydrocarbon steam reforming as $C_2H_4 + H_2O = C_2H_5OH$ in the gas phase and CO oxidation on the catalyst surface), as was experimentally observed [46]. The sensitivity coefficients of the corresponding backward reaction rates are presented in Figure S12.

### 3.4. Temperature distribution estimation of catalyst bed

The condition of the best yield in Fig. 3(a) was thought to be the closest to the optimum temperature. The hint of optimum temperature is known from low-pressure experiments as shown in Figure S13. Figure S13(a) shows that the optimum temperature is around the furnace temperature of 800 °C. Figure S13(c) shows that the outer temperature of catalyst bed can reach around 825 °C which means the reaction temperature inside the catalyst bed will be even higher. An isothermal plug flow reactor was utilized to estimate the reaction zone using the developed kinetic model. Because hydrocarbon reforming

reactions were not included in the surface mechanism, the reaction region was chosen as ca. 3 mm, which is estimated from the temperature profile of 240 ml min^{-1} in Fig. 6(d). Most of the OCM reactions are assumed to take place in the region of catalyst bed length from 14.6 mm to 17.6 mm in Fig. 6(d). The site density is practically difficult to quantify for the catalyst investigated per given volume of the reactor because there is no technique to count the true active site for this type of catalyst in addition to the difficulty controlling the packing of the catalyst in the reactor. In this context, the site density was thought to be the only parameter necessary to obtain an accurate fit. For each site density, the reaction temperature that can just deplete O_2 at the end of the 3 mm reaction region was taken to calculate the residual values for comparison as shown in Fig. 8(a). The site density was controlled below the theoretical maximum site density of 1.51×10^{-8} that is calculated in support information. The reaction temperature was predicted as 885 °C with a site density of 7.31×10^{-10} mol cm^{-2}. The temperature is close to the optimum temperature for the low-pressure condition [25].

Since OCM reaction proceeds via homogeneous-heterogeneous reactions, the reactor model requires suitable adjustment depending on catalyst site density and void fraction. This study shows that the reaching temperature is the most critical parameter to attain highest yield for a given catalyst. Active site density altered either by the loading or the catalyst composition (dilution of Mn-K_2WO_4/SiO_2 is possible by adding Sn, for example) should be carefully tuned to attain the adequate reaction temperatures. The temperature can be further adjusted by setting adequate reaction conditions, such as flow rate and heat dissipation rates. The comprehensive kinetic model developed in this study is used as a core fundamental of developing reactor design for OCM and beyond.

4. Conclusion

With the inclusion of newly added surface elementary steps, encompassing the formation of surface peroxide intermediate, the established microkinetic model successfully replicated the promotional H_2O effects through the OH-mediated pathway, along with the corresponding kinetic data under various reaction conditions. Unlike the lattice oxygen (O*) of metal oxide catalysts (e.g., La_2O_3-CeO_2), transient active oxygen (O_2*) of alkali metal tungstate-based catalyst accelerates OH$\bullet$ production from H_2O and O_2 to selectively abstract the hydrogen from CH_4 into $CH_3\bullet$. Furthermore, strongly exothermic high-pressure conditions were explored for the potential industrial application by using a operando thermal visualization platform equipped with IR camera to measure the temperature distributions of the catalyst bed. The C_{2-4} (C_2)yield were improved up to the maximum, ca. 13.7 (11.8) % at 19.9 % CH_4 conversion with 68.6 (59.1) % selectivities at 901 kPa by decreasing furnace temperature to lead the heat spot to adequate temperature. Too high temperatures caused hydrocarbon reforming to produce CO and H_2. The established model predicts the best average
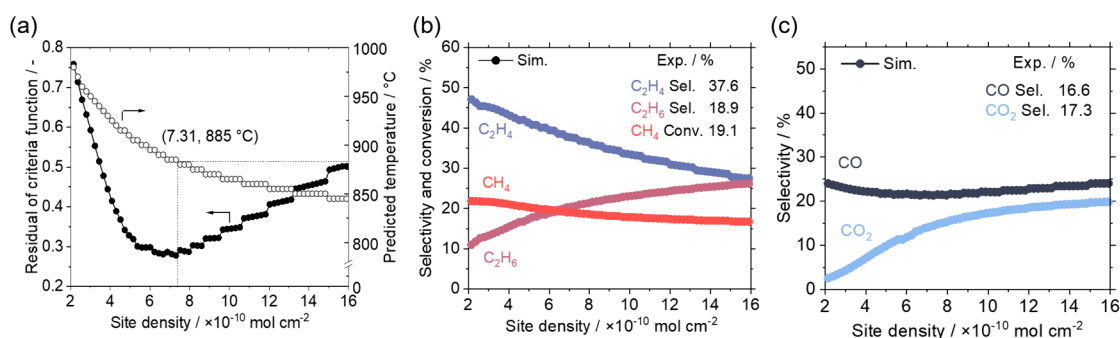
Fig. 8. (a) Residual of criteria function and the temperature as O_2 is just depleted; (b) selectivities of C_2H_4, C_2H_6 and conversion of CH_4; (c) selectivities of CO and CO_2 as a function of site density under the CH_4/O_2 ratio of 6, flow rate of 240 ml min^{-1} without dilution, catalyst amount of 300 mg, pressure of ca. 901 kPa, through the parametric study.

temperature of the catalyst to be ca. 885 °C, which is consistent with the maximum selectivity and yield at low-pressure conditions that can avoid too much exotherms. Finally, the sensitivity analysis under low-pressure and high-pressure conditions showed the importance of surface reactions as well as active site density. The understanding and methodology for the mechanism as well as experimental strategy can be extended to other catalysts and reaction systems. A deep understanding of high-pressure OCM obtained by this study helps to accelerate its use in potential industrial applications.

Associated Content

The support information is available free of charge.

Brunauer-Emmett-Teller (BET) surface area; X-ray Diffraction (XRD) patterns; Scanning electron microscopy (SEM) images; theoretical maximum site density; Thiele Modulus; Weisz-Prater Modulus; Mears' criterion; definitions of selectivity and sensitivity; calibrations for infrared camera; comparisons of high-pressure performances among various catalysts; water effect under high pressure; operando thermal visualizations for blank reactor.

Notes.

The authors declare no competing financial interest.

CRediT authorship contribution statement

Yuhang Yu: Data curation, Writing – original draft. **Keisuke Obata:** Data curation, Formal analysis. **William J. Movick:** Data curation, Formal analysis. **Shintaro Yoshida:** Data curation. **Jose Palomo:** Data curation. **Sean-Thomas B. Lundin:** Formal analysis. **Atsushi Urakawa:** Formal analysis, Validation. **S. Mani Sarathy:** Writing - review & editing, Project administration.. **Kazuhiro Takanabe:** Conceptualization, Formal analysis, Project administration, Supervision, Writing – review & editing.

Declaration of competing interest

The authors declare that they have no known competing financial interests or personal relationships that could have appeared to influence the work reported in this paper.

Data availability

Data will be made available on request.

Appendix A. Supplementary data

Supplementary data to this article can be found online at https://doi.org/10.1016/j.jcat.2024.115414.

References

[1] G.E. Keller, M.M. Bhasin, Synthesis of ethylene via oxidative coupling of methane I. determination of active catalysts, J. Catal. 73 (1982) 9–19, https://doi.org/10.1016/0021-9517(82)90075-6.

[2] T. Ito, J.H. Lunsford, Synthesis of ethylene and ethane by partial oxidation of methane over lithium-doped magnesium oxide, Nature 314 (1985) 721–722.

[3] K.D. Campbell, J.H. Lunsford, Contribution of gas-phase radical coupling in the catalytic oxidation of methane, J. Phys. Chem. 92 (1988) 5792–5796.

[4] J.H. Lunsford, The catalytic oxidative coupling of methane, Angew. Chem. Int. Ed. 34 (1995) 970–980, https://doi.org/10.1002/anie.199509701.

[5] J.A. Labinger, K.C. Ott, Mechanistic studies on the oxidative coupling of methane, J. Phys. Chem. 91 (1987) 2682–2684, https://doi.org/10.1021/j100295a003.

[6] C.A. Mims, R. Mauti, A.M. Dean, K.D. Rose, Radical chemistry in methane oxidative coupling: Tracing of ethylene Secondary reactions with computer models and isotopes, J. Phys. Chem. 98 (1994) 13357–13372, https://doi.org/10.1021/j100101a041.

[7] J.A. Labinger, Oxidative coupling of methane: an inherent limit to selectivity? Catal. Lett. 1 (1988) 371–375, https://doi.org/10.1007/BF00766166.

[8] K. Takanabe, E. Iglesia, Rate and selectivity enhancements mediated by OH radicals in the oxidative coupling of methane catalyzed by $Mn/Na_2WO_4/SiO_2$, Angew. Chem. Int. Ed. 47 (2008) 7689–7693, https://doi.org/10.1002/anie.200802608.

[9] K. Takanabe, E. Iglesia, Mechanistic aspects and reaction pathways for oxidative coupling of methane on $Mn/Na_2WO_4/SiO_2$ catalysts, J. Phys. Chem. C 113 (2009) 10131–10145, https://doi.org/10.1021/jp9001302.

[10] J.G.A. Pacheco Filho, J.G. Eon, M. Schmal, Oxidative coupling of methane on Ce/Na/CaO catalysts, Catal. Lett. 68 (2000) 197–202.

[11] T. Ito, J. Wang, C.H. Lin, J.H. Lunsford, Oxidative dimerization of methane over a lithium-promoted magnesium oxide catalyst, J. Am. Chem. Soc. 107 (1985) 5062–5068, https://doi.org/10.1021/ja00304a008.

[12] K.D. Campbell, H. Zhang, J.H. Lunsford, Methane activation by the lanthanide oxides, J. Phys. Chem. 92 (1988) 750–753, https://doi.org/10.1021/j100314a032.

[13] K. Kwapien, J. Paier, J. Sauer, M. Geske, U. Zavyalova, R. Horn, P. Schwach, A. Trunschke, R. Schlögl, Sites for methane activation on lithium-doped magnesium oxide Surfaces, Angew. Chem. Int. Ed. 53 (2014) 8774–8778, https://doi.org/10.1002/anie.201310632.

[14] D. Noon, A. Seubsai, S. Senkan, Oxidative coupling of methane by nanofiber catalysts, ChemCatChem 5 (2013) 146–149, https://doi.org/10.1002/cctc.201200408.

[15] J. Song, Y. Sun, R. Ba, S. Huang, Y. Zhao, J. Zhang, Y. Sun, Y. Zhu, Monodisperse $Sr–La_2O_3$ hybrid nanofibers for oxidative coupling of methane to synthesize C_2 hydrocarbons, Nanoscale 7 (2015) 2260–2264, https://doi.org/10.1039/C4NR06660J.

[16] H. Wang, C. Yang, C. Shao, S. Alturkistani, G. Magnotti, J. Gascon, K. Takanabe, S. M. Sarathy, A homogeneous-heterogeneous kinetic study of oxidative coupling of methane (OCM) on La_2O_3/CeO_2 catalyst, ChemCatChem 14 (2022) e202200927.

[17] Y. Yu, S.-T.-B. Lundin, K. Obata, S.M. Sarathy, K. Takanabe, Improved Homogeneous−Heterogeneous kinetic mechanism using a Langmuir−Hinshelwood-based microkinetic model for high-pressure oxidative coupling of methane, Ind. Eng. Chem. Res. 62 (2023) 5826–5838.

[18] X.P. Fang, S.B. Li, J.Z. Lin, J.F. Gu, D.X. Yang, Oxidative coupling of methane on W-mn catalysts, J. Mol. Catal. (china) 6 (1992) 427.

[19] Z.C. Jiang, C.J. Yu, X.P. Fang, S.B. Li, H.L. Wang, Oxide/support interaction and surface reconstruction in the sodium tungstate (Na2WO4)/silica system, J. Phys. Chem. 97 (1993) 12870–12875, https://doi.org/10.1021/j100151a038.

[20] A. Palermo, J.P.H. Vazquez, A.F. Lee, M.S. Tikhov, R.M. Lambert, Critical influence of the amorphous silica-to-cristobalite phase transition on the performance of $Mn/Na_2WO_4/SiO_2$ catalysts for the oxidative coupling of methane, J. Catal. 177 (1998) 259–266.

[21] K. Otsuka, A.A. Said, K. Jinno, T. Komatsu, Peroxide anions as possible active species in oxidative coupling of methane, Chem. Lett. 16 (1987) 77–80.

[22] Z. Yu, X. Yang, J.H. Lunsford, M.P. Rosynek, Oxidative coupling of methane over Na_2WO_4/CeO_2 and related catalysts, J. Catal. 154 (1995) 163–173.

[23] K. Takanabe, A.M. Khan, Y. Tang, L. Nguyen, A. Ziani, B.W. Jacobs, A.M. Elbaz, S. M. Sarathy, F.F. Tao, Integrated in situ Characterization of a molten salt catalyst Surface: evidence of sodium peroxide and hydroxyl radical formation, Angew. Chem. Int. Ed. 56 (2017) 10403–10407, https://doi.org/10.1002/anie.201704758.

[24] M. Blocquet, C. Schoemaecker, D. Amedro, O. Herbinet, F. Battin-Leclerc, C. Fittschen, Quantification of OH and HO_2 radicals during the low-temperature oxidation of hydrocarbons by fluorescence assay by gas expansion technique, Proc. Natl. Acad. Sci. u.s.a. 110 (2013) 20014–20017, https://doi.org/10.1073/pnas.1314968110.

[25] Y. Liang, Z. Li, M. Nourdine, S. Shahid, K. Takanabe, Methane coupling reaction in an oxy-steam stream through an OH radical pathway by using supported alkali metal catalysts, ChemCatChem 6 (2014) 1245–1251, https://doi.org/10.1002/cctc.201400018.

[26] K. Takanabe, S. Shahid, Dehydrogenation of ethane to ethylene via radical pathways enhanced by alkali metal based catalyst in oxysteam condition, AIChE J. 63 (2017) 105–110, https://doi.org/10.1002/aic.15447.

[27] M.J. Werny, Y. Wang, F. Girgsdies, R. Schlögl, A. Trunschke, Fluctuating storage of the active phase in a mn-Na2WO4/SiO2 catalyst for the oxidative coupling of methane, Angew. Chem. Int. Ed. 59 (2020) 14921–14926, https://doi.org/10.1002/anie.202004778.

[28] D. Li, S. Yoshida, B. Siritanaratkul, A.T. Garcia-Esparza, D. Sokaras, H. Ogasawara, K. Takanabe, Transient potassium peroxide species in highly selective oxidative coupling of methane over an unmolten $_K2W_O4/Si_O2$ catalyst revealed by in situ Characterization, ACS Catal. 11 (2021) 14237–14248, https://doi.org/10.1021/acscatal.1c04206.

[29] L. Chou, Y. Cai, B. Zhang, J. Niu, S. Ji, S. Li, Oxidative coupling of methane over na-W-Mn/SiO_2 catalysts at elevated pressures, J. Nat. Gas Chem. 11 (2002) 131–136.

[30] L. Chou, Y. Cai, B. Zhang, J. Niu, S. Ji, S. Li, Oxidative coupling of methane over na-mn-W/SiO_2 catalyst at higher pressure, React. Kinet. Catal. Lett. 76 (2002) 311–315.

[31] S. Pak, J.H. Lunsford, Thermal effects during the oxidative coupling of methane over Mn/Na$_2$WO$_4$/SiO$_2$ and Mn/Na2WO4/MgO catalysts, Appl. Catal. A-Gen. 168 (1998) 131–137, https://doi.org/10.1016/S0926-860X(97)00340-2.

[32] C. Karakaya, H. Zhu, C. Loebick, J.G. Weissman, R.J. Kee, A detailed reaction mechanism for oxidative coupling of methane over Mn/Na$_2$WO$_4$/SiO$_2$ catalyst for non-isothermal conditions, Catal. Today 312 (2018) 10–22, https://doi.org/10.1016/j.cattod.2018.02.023.

[33] A. Aseem, G.G. Jeba, M.T. Conato, J.D. Rimer, M.P. Harold, Oxidative coupling of methane over mixed metal oxide catalysts: steady state multiplicity and catalyst durability, Chem. Eng. J. 331 (2018) 132–143, https://doi.org/10.1016/j.cej.2017.08.093.

[34] L. Hu, D. Pinto, A. Urakawa, Catalytic oxidative coupling of methane: heterogeneous or homogeneous reaction? ACS Sustain. Chem. Eng. 11 (2023) 10835–10844, https://doi.org/10.1021/acssuschemeng.3c02088.

[35] Y.S. Su, J.Y. Ying, W.H. Green Jr, Upper bound on the yield for oxidative coupling of methane, J. Catal. 218 (2003) 321–333, https://doi.org/10.1016/S0021-9517(03)00043-5.

[36] M.Y. Sinev, Free radicals in catalytic oxidation of light alkanes: kinetic and thermochemical aspects, J. Catal. 216 (2003) 468–476, https://doi.org/10.1016/S0021-9517(02)00116-1.

[37] J. Sun, J. Thybaut, G. Marin, Microkinetics of methane oxidative coupling, Catal. Today 137 (2008) 90–102, https://doi.org/10.1016/j.cattod.2008.02.026.

[38] R. Gaikwad, H. Reymond, N. Phongprueksathat, P. Rudolf Von Rohr, A. Urakawa, From CO or CO2?: space-resolved insights into high-pressure CO2 hydrogenation to methanol over Cu/ZnO/Al2O3, catal, Sci. Technol. 10 (2020) 2763–2768, https://doi.org/10.1039/D0CY00050G.

[39] D. Li, W.S. Baslyman, S.M. Sarathy, K. Takanabe, Impact of OH radical generator involvement in the gas-phase radical reaction network on the oxidative coupling of methane–a simulation study, Energy Technol. 8 (2020) 1900563, https://doi.org/10.1002/ente.201900563.

[40] M.G. Evans, M. Polanyi, Further considerations on the thermodynamics of chemical equilibria and reaction rates, Trans. Faraday Soc. 32 (1936) 1333–1360, https://doi.org/10.1039/tf9363201333.

[41] V.I. Alexiadis, J.W. Thybaut, P.N. Kechagiopoulos, M. Chaar, A.C. Van Veen, M. Muhler, G.B. Marin, Oxidative coupling of methane: catalytic behaviour assessment via comprehensive microkinetic modelling, Appl Catal B-Environ 150–151 (2014) 496–505, https://doi.org/10.1016/j.apcatb.2013.12.043.

[42] P.W. Oxby, T.A. Duever, P.M. Reilly, Multivariate weighted least squares as an alternative to the determinant criterion for multiresponse parameter estimation, Comput Chem Eng 16 (2003) 63–84, https://doi.org/10.1016/S1570-7946(03)80070-6.

[43] D. Wang, D. Tan, L. Liu, Particle swarm optimization algorithm: an overview, Soft Comput 22 (2018) 387–408, https://doi.org/10.1007/s00500-016-2474-6.

[44] L.C. Anderson, M. Xu, C.E. Mooney, M.P. Rosynek, J.H. Lunsford, Hydroxyl radical formation during the reaction of oxygen with methane or water over basic lanthanide oxide catalysts, J. Am. Chem. Soc. 115 (1993) 6322–6326, https://doi.org/10.1021/ja00067a055.

[45] K.B. Hewett, L.C. Anderson, M.P. Rosynek, J.H. Lunsford, Formation of hydroxyl radicals from the reaction of water and oxygen over basic metal oxides, J. Am. Chem. Soc. 118 (1996) 6992–6997, https://doi.org/10.1021/ja960566g.

[46] H. Komada, K. Obata, D. Li, S.M. Sarathy, K. Takanabe, Consequence of products from oxidative coupling of methane in a non-oxidative high temperature environment, CatalSci. Technol. 13 (2023) 2142–2150, https://doi.org/10.1039/D2CY02145E.